Comput Mech (2007) 40:911–931
DOI 10.1007/s00466-006-0151-9

ORIGINAL PAPER

Heterogeneous upper-bound finite element limit analysis of masonry walls out-of-plane loaded

G. Milani · F. A. Zuccarello · R. S. Olivito · A. Tralli

Received: 29 September 2006 / Accepted: 18 November 2006 / Published online: 10 January 2007
© Springer-Verlag 2006

Abstract A heterogeneous approach for FE upper bound limit analyses of out-of-plane loaded masonry panels is presented. Under the assumption of associated plasticity for the constituent materials, mortar joints are reduced to interfaces with a Mohr–Coulomb failure criterion with tension cut-off and cap in compression, whereas for bricks both limited and unlimited strength are taken into account. At each interface, plastic dissipation can occur as a combination of out-of-plane shear, bending and torsion. In order to test the reliability of the model proposed, several examples of dry-joint panels out-of-plane loaded tested at the University of Calabria (Italy) are discussed. Numerical results are compared with experimental data for three different series of walls at different values of the in-plane compressive vertical loads applied. The comparisons show that reliable predictions of both collapse loads and failure mechanisms can be obtained by means of the numerical procedure employed.

Keywords Masonry · Heterogeneous approach · Out-of-plane loads · FE limit analysis · Reissner–Mindlin plates

G. Milani (✉) · A. Tralli
Department of Engineering, University of Ferrara,
Via Saragat 1, 44100 Ferrara, Italy
e-mail: gmilani@ing.unife.it

F. A. Zuccarello · R. S. Olivito
Department of Structural Engineering,
University of Calabria, 87036 Rende (CS), Italy

1 Introduction

The evaluation of the ultimate load bearing capacity of masonry elements (columns, arches and walls) is a key aspect both for the design of new structures and the assessment of existing buildings.

Furthermore, load bearing masonry walls are simultaneously subjected to both in-plane loads (self weight) and out-of-plane actions (earthquakes, wind, explosions).

While masonry behavior subjected to in-plane actions has been widely investigated, relatively few papers devoted to the analysis of out-of-plane actions have been presented in the recent past in the technical literature (see for instance Lourenço [13], Milani et al. [17], Cecchi et al. [4]), even if the importance of the problem was stressed for the first time two centuries ago by Rondelet [23], who was probably the first researcher able to catalogue out-of-plane collapses.

Several surveys conducted in Italy after the Friuli (1976), Umbria-Marche (1997–1998) and Molise (2002) earthquakes confirmed both that the lack of out-of-plane strength is a primary cause of failure in different forms of masonry (Spence and Coburn [26], Borri et al. [1]) and that collapses can be caused by an inadequate toothing between perpendicular walls.

On the other hand, laboratory tests conducted on brick masonry structures out-of-plane loaded (see for instance Chee Liang [7], Gazzola and Drysdale [8], Gazzola et al. [9], Guggisberg and Thurlimann [10] and [11], van der Pluijm [28] and West et al. [29]) have shown that failure takes place along a well-defined pattern of lines, which usually follows the joints' disposition. Therefore, it is commonly accepted that mortar joints, or more precisely the interfaces between bricks and mortar,

have a much lower strength than that of the bricks, thus representing preferential planes of weakness along which cracks propagate. This evidence inspired approximate analytical solutions based both on the yield line theory and on the fracture line theory (Sinha [24], BS 5628 [2], Eurocode 6 [5]).

Furthermore, another important aspect that should be better investigated is the combined interaction of membrane and flexural loads. As a matter of fact, in-plane loads increase both the ultimate out-of-plane strength and the ductility of masonry, and bring additional complexity to the structural analysis.

Numerical models based on the classic Kirchhoff-Love theory, able to take into account the influence of membrane loads and devoted to the analysis of masonry in the inelastic range, have already been presented by Lourenço [13], Casolo [3] and Milani et al. [16].

On the other hand, it has been shown (Milani et al. [15–17]) that classic limit analysis theorems can be profitably used for the prediction both of collapse loads and failure mechanisms of masonry structures in- and out-of-plane loaded. In this framework, different numerical models for the in-plane analysis of masonry have been proposed in past literature, based either on homogenization theory (see Milani et al. [15,16]) or on a separate modeling of bricks and mortar joints (see Sutcliffe et al. [27]).

However, it is worth noting that load bearing walls are relatively thick and, as a matter of fact, many construction codes impose for them a minimum slenderness, as for instance the recent Italian O.P.C.M. 3431 2005 [21], in which the upper bound slenderness is fixed, respectively, equal to 12 for artificial bricks and 10 for natural blocks masonry. In spite of this consideration, only very few papers devoted to the analysis of thick masonry walls out-of-plane loaded have been presented, see for instance Cecchi et al. [4] and Orduna and Lourenço [22].

In light of these considerations, in this paper, a heterogeneous approach is used in combination with limit analysis concepts for the study of both thin and thick masonry plates. A FE upper bound heterogeneous limit analysis model is presented based on a triangular discretization of the domain, where joints are reduced to interfaces with frictional behavior and limited tensile and compressive strength. Out-of-plane velocities interpolation is assumed to vary linearly inside each element and possible jumps of velocities can occur at the interface between adjacent triangles. In this way, no dissipation is possible in continuum, whereas at each interface (mortar or brick interfaces), plastic dissipation can occur as a combination of out-of-plane shear, bending and torsion.

In order to assess the reliability of the numerical model proposed, a set of experimental analyses on $100 \times 100\,\mathrm{cm}^2$ in scale models has been conducted at the University of Calabria (Italy) on three series of dry-joints masonry walls out-of-plane loaded. To this aim, the experimental equipment proposed in [20] has been used. All the series have been loaded up to failure by means of a concentrated horizontal force, after the application of three different sets of vertical compressive loads, respectively, equal to 13, 10 and 7 kN. The first series (A) was fixed to a steel frame on two perpendicular edges, whereas the second (B) and the third (C) were clamped on three edges. Series C differs from series B only for the point of application of the horizontal load, which is eccentric in Series B and centric in Series C.

The reliability of the numerical procedure adopted is demonstrated by the good correspondence between the experimental data and the numerical predictions.

2 Heterogeneous upper bound FE limit analysis of masonry walls out-of-plane loaded

In this section, a FE kinematic limit analysis model for the analysis of both thick and thin masonry walls is presented. Reissner–Mindlin plate hypotheses are adopted, allowing plastic dissipation for bending moment and torsion as well as out-of-plane shear.

The FE formulation is based on a triangular discretization of the wall, constituted by a regular assemblage of bricks disposed in running bond texture. Hence, each brick is meshed at least using four triangular elements, as shown in Fig. 1, in order to follow the actual disposition of the interfaces between adjacent bricks, i.e., dry-joints.

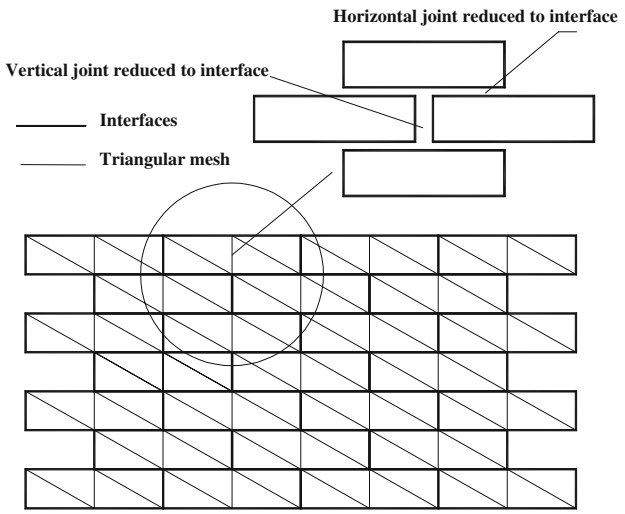

Fig. 1 Heterogeneous triangular discretization

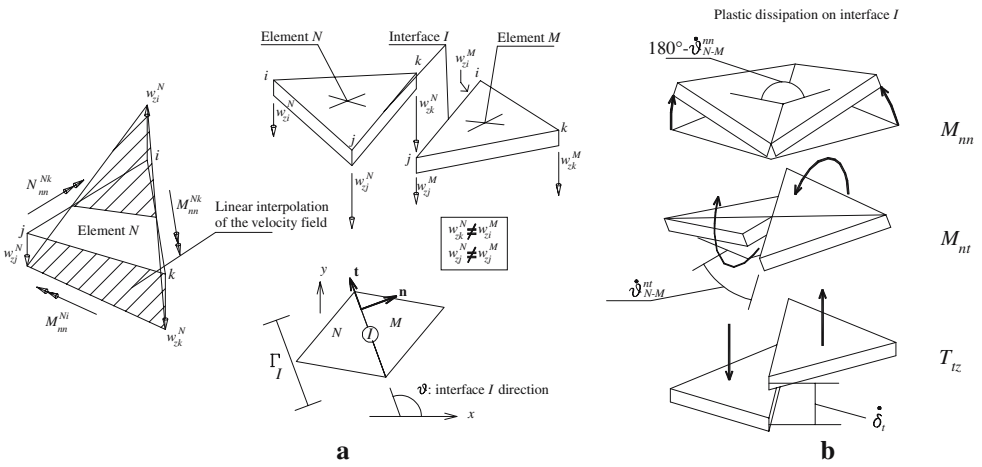

Fig. 2 Reissner-Mindlin FE kinematic limit analysis element. **a** Field of velocities and discontinuity at each interface between adjacent triangles. **b** Possible plastic dissipation at the interface due to bending moment, torsion and shear

For each element E, one out-of-plane velocity unknown w_{zi}^E per node i is introduced, so that the velocity field is linear inside each element. Differently from a well known elastic FE discretization, several nodes may share the same coordinate, being each node associated with only one element. In this way, at each interface between adjacent triangles, possible jumps of velocities can occur.

Being the velocities interpolation inside each element linear, plastic dissipation can occur only at the interface between adjacent elements M and N.

At each interface M and N, both constant bending rotation rates $\dot{\vartheta}_{N-M}^{nn}$ and a torsional rotation rates $\dot{\vartheta}_{N-M}^{nt}$ can occur. Furthermore, an out-of-plane jump of velocities $\dot{\delta}_t$ which varies linearly along the interface is also considered. $\dot{\vartheta}_{N-M}^{nn}$, $\dot{\vartheta}_{N-M}^{nt}$ and $\dot{\delta}_t$ can be easily evaluated making use of the following linear relation between nodal velocities of adjacent elements M and N (see Fig. 2):

$$\begin{aligned}
&\dot{\boldsymbol{\theta}}_N = \mathbf{B}_N \mathbf{w}_z^N \\
&\dot{\vartheta}_{N-M}^{nt} = \frac{w_{zj}^M - w_{zi}^M}{\Gamma_I} - \frac{w_{zj}^N - w_{zk}^N}{\Gamma_I} \\
&\dot{\delta}_t = \left(w_{zj}^M - w_{zj}^N\right) + \frac{x_I}{\Gamma_I}\left[\left(w_{zi}^M - w_{zk}^N\right) - \left(w_{zj}^M - w_{zj}^N\right)\right] \\
&\quad x_I \in \left[0 \quad \Gamma_I\right]
\end{aligned} \tag{1}$$

where

$$\mathbf{w}_z^N = \left[\begin{array}{ccc} w_{zi}^N & w_{zj}^N & w_{zk}^N \end{array}\right]^T;$$

$$\mathbf{B}_N = \frac{1}{2A_N}\left[\begin{array}{ccc} \dfrac{b_i b_i + c_i c_i}{l_i} & \dfrac{b_i b_j + c_i c_j}{l_i} & \dfrac{b_i b_k + c_i c_k}{l_i} \\ \dfrac{b_j b_i + c_j c_i}{l_j} & \dfrac{b_j b_j + c_j c_j}{l_j} & \dfrac{b_j b_k + c_j c_k}{l_j} \\ \dfrac{b_k b_i + c_k c_i}{l_k} & \dfrac{b_k b_j + c_k c_j}{l_k} & \dfrac{b_k b_k + c_k c_k}{l_k} \end{array}\right],$$

$$\text{with } b_i = y_j - y_k, \quad c_i = x_k - x_j$$

and A_N is the element area; $\dot{\theta}_N = \left[\begin{array}{ccc} \dot{\vartheta}_i^N & \dot{\vartheta}_j^N & \dot{\vartheta}_k^N \end{array}\right]^T$ are the side normal rotation rates, linked with $\dot{\vartheta}_{N-M}^{nn}$ by means of the linear equation $\dot{\vartheta}_{N-M}^{nn} = \dot{\vartheta}_i^N - \dot{\vartheta}_i^M$; Γ_I is the interface length.

Power dissipated at each interface between adjacent triangles can be evaluated following a general approach recently presented in the technical literature for the limit analysis of 3D and plane-strain problems (Krabbenhoft et al. [12]) and taking into account that three different elementary interface plastic dissipations can occur, related, respectively, to shear T_{nt}, bending moment M_{nn} and torsion M_{nt}, as illustrated in Fig. 2. Consequently, a linearization of the interface failure surface $\Phi(T_{tn}, M_{nt}, M_{nn})$ is required. To this aim, the interfaces between adjacent triangles are discretized making use of prismatic equilibrated elements, as illustrated in the following section. Finally, it is worth noting that the FE approach here adopted strongly differs from the classic Munro and Da Fonseca [18] upper bound finite element. In [18], in fact, jumps of velocities at the interfaces between adjacent triangles are not allowed, therefore plastic dissipation is due only to bending rotation rates $\dot{\vartheta}_{N-M}^{nn}$.

2.1 A static approach for the determination of the $\Phi(T_{tn}, M_{nt}, M_{nn})$ interface failure surface

In this section, a micro-mechanical approach for the evaluation of the $\Phi(T_{tn}, M_{nt}, M_{nn})$ interfaces failure surface is presented. The model is based on a FE limit analysis procedure in which equilibrium inside each element, equilibrium at the interfaces between adjacent elements and stress admissibility at each node are imposed. In this way, a lower bound approximation of the $\Phi(T_{tn}, M_{nt}, M_{nn})$ actual interface failure surface is obtained by means of a simple linear programming problem. For

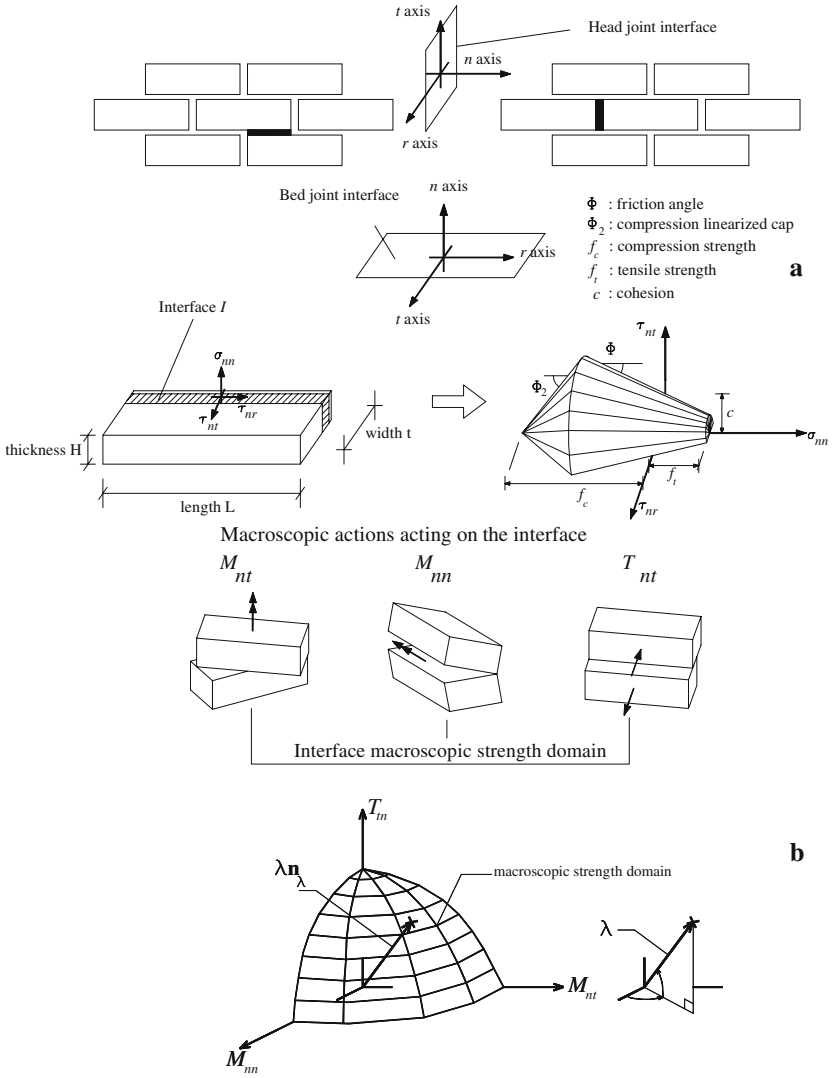

Fig. 3 Stresses acting on head and bed joint interfaces and failure surface adopted for each point of the joints (**a**) macroscopic strength domain of joints and meaning of $\mathbf{n}_\lambda$ in the space $T_{tn} - M_{nn} - M_{nt}$ (**b**)

each interface I, we assume that only normal stress σ_{nn} and two tangential stresses τ_{nt} and τ_{nr} along two assigned perpendicular directions act, as shown in Fig. 3. Following a classic formulation proposed by Sloan [25], the interface is discretized along its length, width and thickness making use of triangular prismatic elements. A typical mesh for a $L \times t = 8.1 \times 4\,\text{cm}^2$ interface is shown in Fig. 4a, where a suitable local $t - r - n$ frame of reference with origin corresponding to the centroid of the interface is also shown. Finally, a double row of elements along the infinitesimal thickness of the interface is adopted.

In order to secure internal equilibrium for each element, we assume a variation of τ_{nt} and τ_{nr} fields linear in r and t and constant in n. On the other hand σ_{nn} is assumed constant in r and t and linearly variable in n. In this way, equilibrium with zero body forces is automatically guaranteed along r and t directions ($\partial\tau_{nt}/\partial n = 0$, i.e., τ_{nt} constant in n; $\partial\tau_{nr}/\partial n = 0$, i.e., τ_{nr} constant in n).

Differently from the elements used in a displacement finite element analysis, several nodes may share the same coordinate, being each node associated with only one element. In this way, statically admissible stress discontinuities can occur at shared edges between adjacent elements.

Denoting by N_E the number of elements in the mesh, the number of nodes is $6N_E$ and, with the assumptions adopted for the stress fields, $8N_E$ are the total unknown stresses (three τ_{nt} and three τ_{nr} stresses, one for each node k of the triangular base of the element and two σ_{nn}^E per element, one for each base of the prism, as shown in Fig. 4b).

The eight unknown stress parameters of the element have to fulfil the third internal equilibrium equation $\partial\tau_{nt}/\partial t + \partial\tau_{nr}/\partial r + \partial\sigma_{nn}/\partial n = 0$ for each element, which

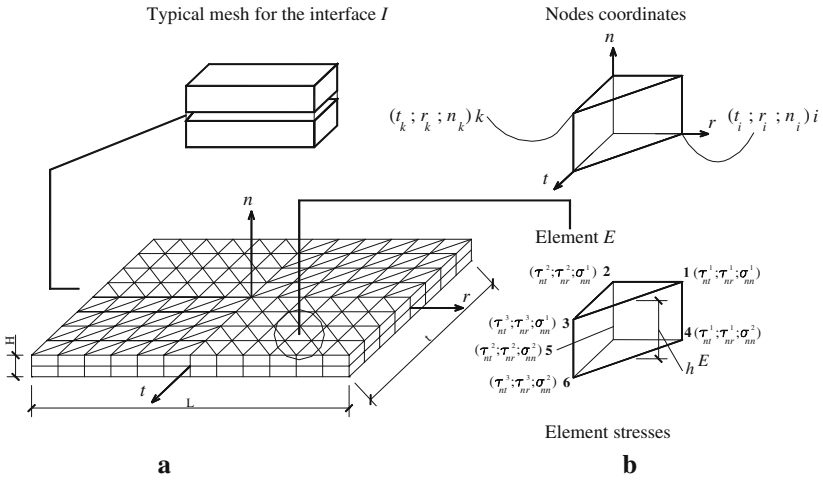

Fig. 4 Typical mesh assumed for the mortar interface (**a**) and stress assumed linear element used in the lower bound limit analysis (**b**)

is not a-priori satisfied. With the stress interpolation adopted throughout each element, the following equilibrium equation has to be imposed:

$$\mathbf{A}^E \boldsymbol{\sigma}^E = 0 \tag{2}$$

where $\mathbf{A}^E = [\eta_1/2A \quad \zeta_1/2A \quad \eta_2/2A \quad \zeta_2/2A \quad \eta_3/2A \quad \zeta_3/2A \quad 1/h^E \quad \sigma^2_{nn}/h^E]$ with $\zeta_i = t_j - t_k$, $\eta_i = r_k - r_j$ (Fig. 4), A is the upper (lower) triangle face area, i, j, $k = 1, 2, 3$, h^E is the prism height; $\boldsymbol{\sigma}^E = [\tau^1_{nt} \quad \tau^1_{nr} \quad \tau^2_{nt} \quad \tau^2_{nr} \quad \tau^3_{nt} \quad \tau^3_{nr} \quad \sigma^1_{nn} \quad \sigma^2_{nn}]^{\mathrm{T}}$.

Since the stress variation inside each element is linear, one equality constraint per element is written on the nodal stresses.

Furthermore, additional constraints on the nodal stresses at the edges of adjacent elements are imposed in order to secure interfacial equilibrium. To this aim, the continuity of the tangential τ_q and normal σ_{nn} stresses between adjacent elements is imposed, where τ_q represents the tangential stress at the interface I^{M-N} between elements $M-N$, Fig. 5. Since only vertical and horizontal interfaces are present in the mesh adopted (Fig. 4), for the vertical interfaces equilibrium involves only τ_q (Fig. 5a), whereas for the horizontal interfaces only σ_{nn} contribution is present (Fig. 5b). Consequently, for a vertical interface, it is necessary to enforce the continuity of τ_q in the initial and final points of the interface I^{M-N} (Fig. 5a), i.e.,

$$\tau_q^N\Big|_1 = \tau_q^M\Big|_2 ; \quad \tau_q^N\Big|_3 = \tau_q^M\Big|_4 \tag{3}$$

It is worth noting that τ_q results as a linear combination between τ^k_{nt} and τ^k_{nr} (i.e. $\tau_q = \tau^k_{nt} \sin(\vartheta^I) - \tau^k_{nr} \cos(\vartheta^I)$, where ϑ^I is the angle between t axis and I^{M-N} interface). By means of trivial algebra, Eq. (3) can be re-written in matrix form as follows:

$$\mathbf{A}^I \boldsymbol{\sigma}^I = \mathbf{b}^I \tag{4}$$

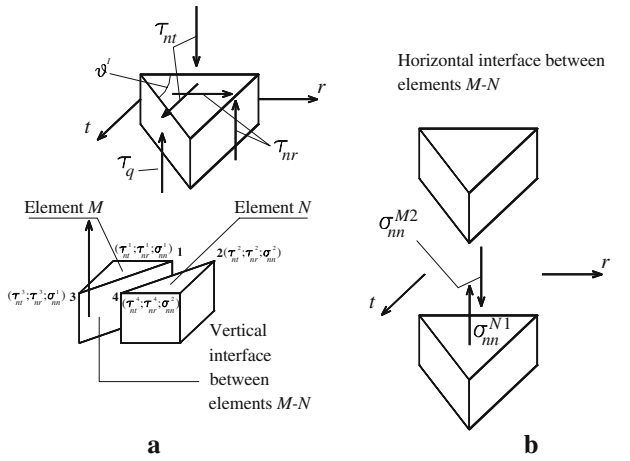

Fig. 5 Continuity of the stress vector on interfaces between adjacent elements. **a** Vertical interface, **b** horizontal interface

where

$$\mathbf{A}^I = \begin{bmatrix} \mathbf{T}^I & -\mathbf{T}^I & \mathbf{0} & \mathbf{0} \\ \mathbf{0} & \mathbf{0} & \mathbf{T}^I & -\mathbf{T}^I \end{bmatrix},$$

$$\mathbf{T}^I = \begin{bmatrix} \sin(\vartheta^I) & -\cos(\vartheta^I) \end{bmatrix};$$

$$\boldsymbol{\sigma}^I = \begin{bmatrix} \tau^1_{nt} & \tau^1_{nr} & \tau^2_{nt} & \tau^2_{nr} & \tau^3_{nt} & \tau^3_{nr} & \tau^4_{nt} & \tau^4_{nr} \end{bmatrix}^T;$$

$\mathbf{0}$ and $\mathbf{b}^I$ are 1×2 vectors of all zeros.

In this way, two equality constraints are generated for each vertical interface.

Similarly, for a horizontal interface, an equation is required to secure σ_{nn} continuity in each point of the interface (Fig. 5b), i.e.:

$$\sigma^{M2}_{nn} = \sigma^{N1}_{nn} \tag{5}$$

Boundary conditions constraints are further imposed both on τ_{nt}, equal to zero at the edges of the interface I parallel to r axis, and on τ_{nr}, equal to zero at the edges of the interface I parallel to t.

Static admissibility is imposed in correspondence to each node of each element and involves only $\boldsymbol{\sigma}^{(k)}$ vector of nodal stresses ($\boldsymbol{\sigma}^{(k)} = [\sigma_{nn}^k; \tau_{nt}^k; \tau_{nr}^k]$), once that a linearization of the failure surface $\phi = \phi(\boldsymbol{\sigma}^{(k)})$ for each node of the interface is provided.

In general, it is stressed that any non-linear failure criterion $\phi = \phi(\boldsymbol{\sigma}^{(k)})$ for joints can be used for the model at hand. As experimental evidence shows, basic failure modes for masonry walls with weak mortar are a mix of sliding along the joints (a), direct tensile splitting of the joints (b) and compressive crushing at the interface between mortar and bricks (c). These modes can be reproduced well when a Mohr-Coulomb failure criterion combined with tension cut-off and cap in compression is adopted, as suggested by Lourenço and Rots [14].

In order to treat the problem in the framework of linear programming, within each node (k) of each element, a piecewise linear approximation of the failure surface $\phi = \phi(\boldsymbol{\sigma}^{(k)})$ is adopted, constituted by n_{lin} planes of equation $\mathbf{A}_i^{I^T} \boldsymbol{\sigma}^{(k)} = c_i^I \quad 1 \leq i \leq n_{lin}$, where $\mathbf{A}_k^{I^T}$ is a 1×3 vector of coefficients and c_k^I is the right hand side of the kth linearization plane, see Fig. 3a.

It is stressed that, in order to obtain a lower bound estimation of the interface failure surface, three additional equilibrium equations involving macroscopic actions T_{tn}, M_{nn} and M_{nt} and (integrated) internal stresses are further imposed, once that an optimization direction $\mathbf{n}_\lambda$ is a priori fixed in the $T_{tn} - M_{nn} - M_{nt}$ space (Fig. 3b).

In this way, the following linear optimization problem is obtained:

$$\begin{cases} \max(\lambda) \\ \text{subject to} \begin{cases} N_{22} = \int_\Gamma \sigma_{nn} \mathrm{d}t \ \mathrm{d}r \\ M_{nn} = \lambda \mathbf{n}_\lambda(1) = \int_\Gamma \sigma_{nn} r \mathrm{d}t \ \mathrm{d}r \\ M_{nt} = \lambda \mathbf{n}_\lambda(2) = \int_\Gamma \tau_{nt} r \mathrm{d}t \ \mathrm{d}r \\ T_{tn} = \lambda \mathbf{n}_\lambda(3) = \int_\Gamma \tau_{nr} \mathrm{d}t \ \mathrm{d}r \\ \mathbf{A}^{I^T} \boldsymbol{\sigma}^{(k)} \leq \mathbf{c}^{(k)} \quad \forall(k) \\ \mathbf{A}^{\mathrm{eq}^T} \tilde{\boldsymbol{\sigma}} = \mathbf{b}^{\mathrm{eq}} \end{cases} \end{cases} \tag{6}$$

Where λ is the limit load in the space $T_{tn} - M_{nn} - M_{nt}$, see Fig. 3b; $\mathbf{n}_\lambda$ is the optimization direction. It is worth noting that, for an accurate lower bound estimation of the failure surface, several $\mathbf{n}_\lambda$ directions should be investigated. N_{22} is the membrane load perpendicular to the interface direction. It is worth underlining that, for the sake of simplicity, N_{22} is kept constant. This implies that for bed joints we assume N_{22} equal to the applied in-plane vertical compressive load, whereas for head joints we assume N_{22} equal to zero. $\mathbf{A}^{\mathrm{eq}}$ is the overall constraints matrix and collects equilibrium equations in continuum, on interfaces between adjacent elements, and boundary conditions, whereas $\mathbf{b}^{\mathrm{eq}}$ is a vector collecting equalities right hand sides; $\tilde{\boldsymbol{\sigma}}$ is the vector of assembled nodal stress parameters.

It is stressed that torsional moment is evaluated, in the framework of the Reissner-Mindlin plate hypothesis, considering only the contribution of τ_{nt}. Nevertheless, no conceptual difficulties occur when τ_{nr} stresses are taken into account, i.e., when $M_{nt} = \lambda \mathbf{n}_\lambda(2) = \int_\Gamma \tau_{nt} r \mathrm{d}t$, $\mathrm{d}r - \int_\Gamma \tau_{nr} t \mathrm{d}t \ \mathrm{d}r$. In the latter case, a 3D behavior for the interface is obtained and classical analytical limit analysis solutions (as for instance the fully plastic torsion of a rectangular section, Nadai [19]) can be well approximated.

Finally, it is worth noting that the optimization problem (6), solved for several values of $\mathbf{n}_\lambda$ optimization directions, allows to obtain the $\Phi(T_{tn}, M_{nt}, M_{nn})$ joints failure surface, as well as $M_{nn} - M_{nt}, T_{tn} - M_{nn}$ and $T_{tn} - M_{nn}$ failure sections.

In order to test the reliability of the static approach proposed, in Table 1, a comparison between the results here obtained and a simplified and heuristic kinematic approach adopted in [22] is reported for pure bending moment, pure torsion and pure shear at failure. Interface dimensions are fixed as $L \times t = 30 \times 20\,\mathrm{cm}^2$, whereas a linearized Mohr-Coulomb failure criterion with cohesion $c = 0.001\,\mathrm{N/mm}^2$ and friction angle $\Phi = 35°$ are assumed for the interface. Finally a vertical compressive load equal to $0.004\,\mathrm{N/mm}^2$ is imposed. As can be noted, the comparison shows perfect agreement with the kinematic approach, suggesting that the FE model proposed can be used for practical purposes.

In Fig. 6, a $T_{tn} - M_{nn} - M_{nt}$ typical joint failure surface for different values of the in-plane compressive load is shown assuming for mortar both a Mohr-Coulomb failure criterion (Fig. 6a: cohesion $c = 0.01\,\mathrm{daN/cm}^2$, friction angle $\Phi = 30°$, membrane compressive load $N_{22} = 56.7\,\mathrm{daN}$) and a linearized Lourenço and Rots [14] failure criterion (Fig. 6b: $c = 0.01\,\mathrm{daN/cm}^2, \Phi = 30°, f_c = 5\,\mathrm{daN/cm}^2, f_t = c/\tan(\Phi), \Phi_2 = 45°, N_{22} = 56.7\,\mathrm{daN}$; Fig. 6c: $c = 0.01\,\mathrm{daN/cm}^2, \Phi = 30°, f_c = 25\,\mathrm{daN/cm}^2$,

Table 1 Comparison between the present model and a kinematic approach [22] for the evaluation of ultimate bending moment, torsion and shear for a typical mortar interface (interface dimensions $L \times t = 30 \times 20\,\mathrm{cm}^2$, interface cohesion $c = 0.001\,\mathrm{N/mm}^2$ and friction angle $\Phi = 35°$, vertical membrane compressive load $0.004\,\mathrm{N/mm}^2$)

Model	Present	Kinematic approach
Pure M_{nn} (daN cm)	231.7	240
Pure M_{nt} (daN cm)	154	160
Pure T_{nt} (daN)	16.1	16.8

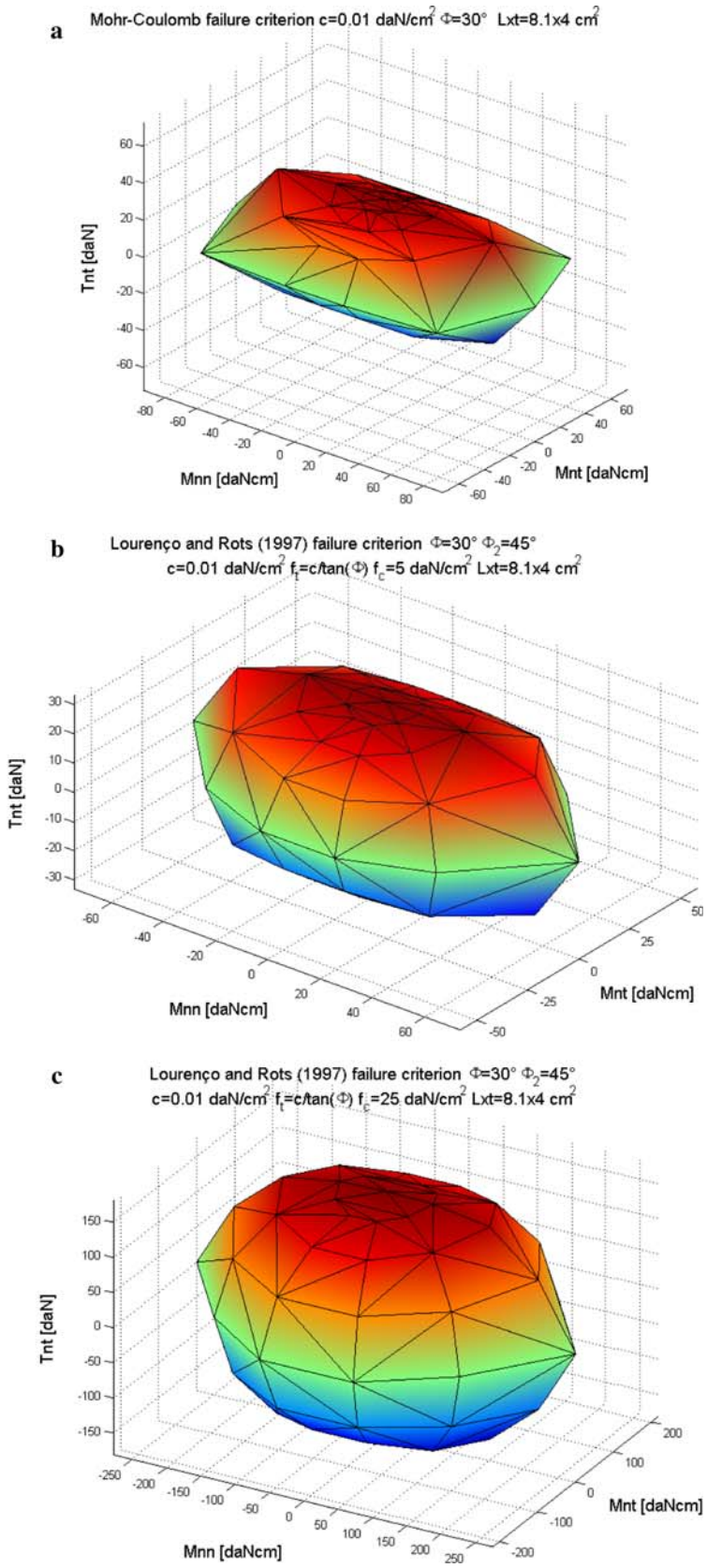

Fig. 6 $T_{tz} - M_{nn} - M_{nt}$ interface failure surface for mortar in presence of a compressive load. **a** Mohr–Coulomb failure criterion, $N_{22} = 56.7$ daN. **b** Lourenço and Rots [14] failure criterion ($c = 0.01$ daN/cm^2, $\Phi = 30°$, $f_c = 5$ daN/cm^2, $f_t = c/\tan(\Phi)$, $\Phi_2 = 45°$) $N_{22} = 56.7$ daN. **c** Lourenço and Rots [14] failure criterion ($c = 0.01$ daN/cm^2, $\Phi = 30°$, $f_c = 25$ daN/cm^2, $f_t = c/\tan(\Phi)$, $\Phi_2 = 45°$) $N_{22} = 631.8$ daN

$f_t = c/\tan(\Phi), \Phi_2 = 45°, N_{22} = 631.8\,\text{daN}$). The difference among the failure surfaces, due both to the strength domain adopted and to the vertical membrane compressive load, is worth noting.

Similarly, in Fig. 7a–c $M_{nn} - M_{nt}$, $M_{nn} - T_{nt}$ and $M_{nt} - T_{nt}$ interface failure surface sections are reported progressively increasing the in-plane compressive load acting on the interface. In this case, a Mohr–Coulomb failure criterion with cohesion $c = 0.01\,\text{daN/cm}^2$ and friction angle $\Phi = 30°$ is adopted, so reproducing a typical dry-joint interface. As can be noted, an increase of the membrane compressive load always results in an increase of the $T_{tn} - M_{nn} - M_{nt}$ ultimate strength of the interface, as a consequence of the unlimited compressive strength of the interface. Obviously, this is not in agreement with experimental evidence, which shows (a) the existence of an optimal compressive load for which failure moments reach a maximum and (b) limited compressive strength of the joints. Thus, a model with compressive cap is able to better reproduce these phenomena, as shown in Fig. 8, where the same results shown in Fig. 7 are reported adopting a Lourenço and Rots [14] failure criterion [cohesion $c = 0.01\,\text{daN/cm}^2$, friction angle $\Phi = 30°$, compressive cap $f_c = 5\,\text{daN/cm}^2$ $\Phi_2 = 45°$, tension cutoff $f_t = c/\tan(\Phi)$].

2.2 The heterogeneous upper bound limit analysis approach

In this section, a heterogeneous upper bound limit analysis approach suitable for the evaluation of collapse loads of masonry walls out-of-plane loaded is presented.

Figure 9a shows the heterogeneous mesh used in this paper for the analysis of experimentally tested dry-joint walls. The mesh used is constituted by 1,375 triangular elements and 2,592 nodes. In Fig. 9b, a zoomed detail of the heterogeneous mesh in correspondence to two corners of the walls and bricks disposition is reported. Furthermore, in Fig. 9c and d, it is stressed how plastic dissipation can occur both at the interfaces between adjacent bricks (i.e., inside each mortar/dry joint) and at the internal brick interfaces, meaning that a general approach in which bricks failure is taken into account can be adopted.

Solving the optimization problem (6) for several directions $\mathbf{n}_\lambda$, it is possible to obtain, by means of well known numerical procedures based on Delaunay tessellation, a linearization with m planes of the interface failure surface $\Phi(T_{zt}, M_{nt}, M_{nn})$ as follows:

$$\mathbf{A}_I^{in}\hat{\mathbf{M}} \le \mathbf{C}_I^{in} \tag{7}$$

where $\hat{\mathbf{M}} = \left[T_{zt}\ M_{nt}\ M_{nn}\right]$, $\mathbf{A}_I^{in}$ is a $m \times 3$ vector of coefficients and $\mathbf{C}_I^{in}$ is a vector of length m representing the right hand sides of the linearization planes.

Making use of Eqs. (1) and (6), internal power dissipated at each interface between adjacent triangles can be evaluated by means of the following expression:

$$\begin{aligned} P^I &= \Gamma_I\left(M_{nn}\dot{\vartheta}_{nn} + M_{nt}\dot{\vartheta}_{nt}\right) + \frac{\Gamma_I}{2}\left(T_{zt}^{Ii}\dot{\delta}_{zt}^{Ii} + T_{zt}^{If}\dot{\delta}_{zt}^{If}\right) \\ &= \frac{\Gamma_I}{2}\sum_{q=1}^{m} C_{I,q}^{in}\left(\dot{\lambda}_{Ii}^{(q)} + \dot{\lambda}_{If}^{(q)}\right) \end{aligned} \tag{8}$$

where $\dot{\lambda}_{Ii}^{(q)}$ and $\dot{\lambda}_{If}^{(q)}$ represent respectively the qth plastic multiplier rate of the initial (i) and final (f) point of the interface I, being the variation of plastic multiplier rates on interfaces linear; $\dot{\delta}_{zt}^{Ii}$ and $\dot{\delta}_{zt}^{If}$ are the jumps of velocities between elements N and M in correspondence to the initial (i) and final (f) point of the interface I, respectively.

As can be noted, in Eq. (8) the well known normality rule $\dot{\vartheta}_{nn} = \dot{\lambda}_I \partial\Phi/\partial M_{nn} = \sum_{q=1}^{m} \dot{\lambda}_I^{(q)} \mathbf{A}_I^{in}(q,\ 1)$ has been used. Hence, additional equality constraints for the optimization problem are added.

On the other hand, external power dissipated can be written as:

$$P^{\text{ex}} = \left(\mathbf{P}_0^{\text{T}} + \lambda\mathbf{P}_1^{\text{T}}\right)\mathbf{w} \tag{9}$$

where $\mathbf{P}_0$ is the vector of equivalent lumped permanent loads; λ is the load multiplier, $\mathbf{P}_1$ is the vector of lumped variable loads and $\mathbf{w}$ is the vector of assembled nodal velocities.

As the amplitude of the failure mechanism is arbitrary, a further normalization condition in the form $\mathbf{P}_1^{\text{T}}\mathbf{w} = 1$ is usually introduced.

Hence, the external power becomes linear in $\mathbf{w}$ and λ:

$$P^{\text{ex}} = \mathbf{P}_0^{\text{T}}\mathbf{w} + \lambda. \tag{10}$$

After elementary assemblage operations and considering Eqs. (1), (8) and (10), the following optimization problem is obtained at a structural level:

$$\begin{cases} \min\left\{\sum_{i=1}^{n^I} P^I - \mathbf{P}_0^{\text{T}}\mathbf{w}\right\} \\ \text{such that}\begin{cases} \mathbf{A}^{\text{eq}}\mathbf{U} = \mathbf{A}^{\text{eq}}\left[\mathbf{w}\ \ \tilde{\dot{\boldsymbol{\theta}}}_{nn}\ \ \tilde{\dot{\boldsymbol{\theta}}}_{nt}\ \ \tilde{\dot{\boldsymbol{\delta}}}_{zt}\ \ \dot{\boldsymbol{\lambda}}^{I,\text{ass}}\right] = \mathbf{b}^{\text{eq}} \\ \dot{\boldsymbol{\lambda}}^{I,\text{ass}} \ge \mathbf{0} \end{cases} \end{cases} \tag{11}$$

where $\mathbf{C}_E^T$ and $\mathbf{C}_I^T$ are the (assembled) right-hand sides of the inequalities which determine the linearized failure surface of the homogenised material, respectively,

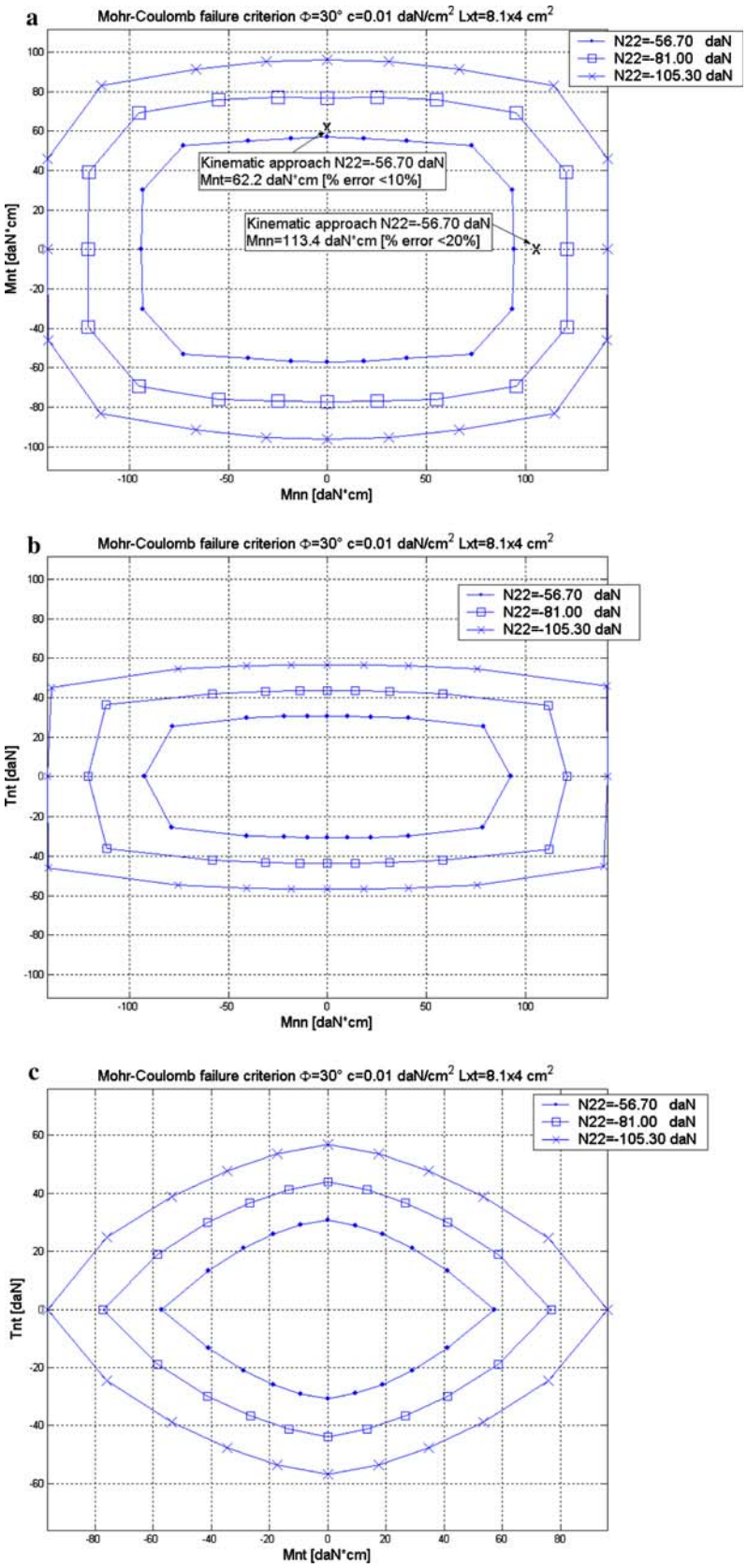

Fig. 7 Interface failure surface sections in presence of different in-plane compressive loads. **a** $M_{nn} - M_{nt}$ sections. **b** $M_{nn} - T_{nt}$ sections, **c** $M_{nt} - T_{nt}$ sections. For the interface, a Mohr–Coulomb failure criterion with cohesion $c = 0.01\,\text{daN/cm}^2$ and friction angle $\Phi = 30°$ is assumed

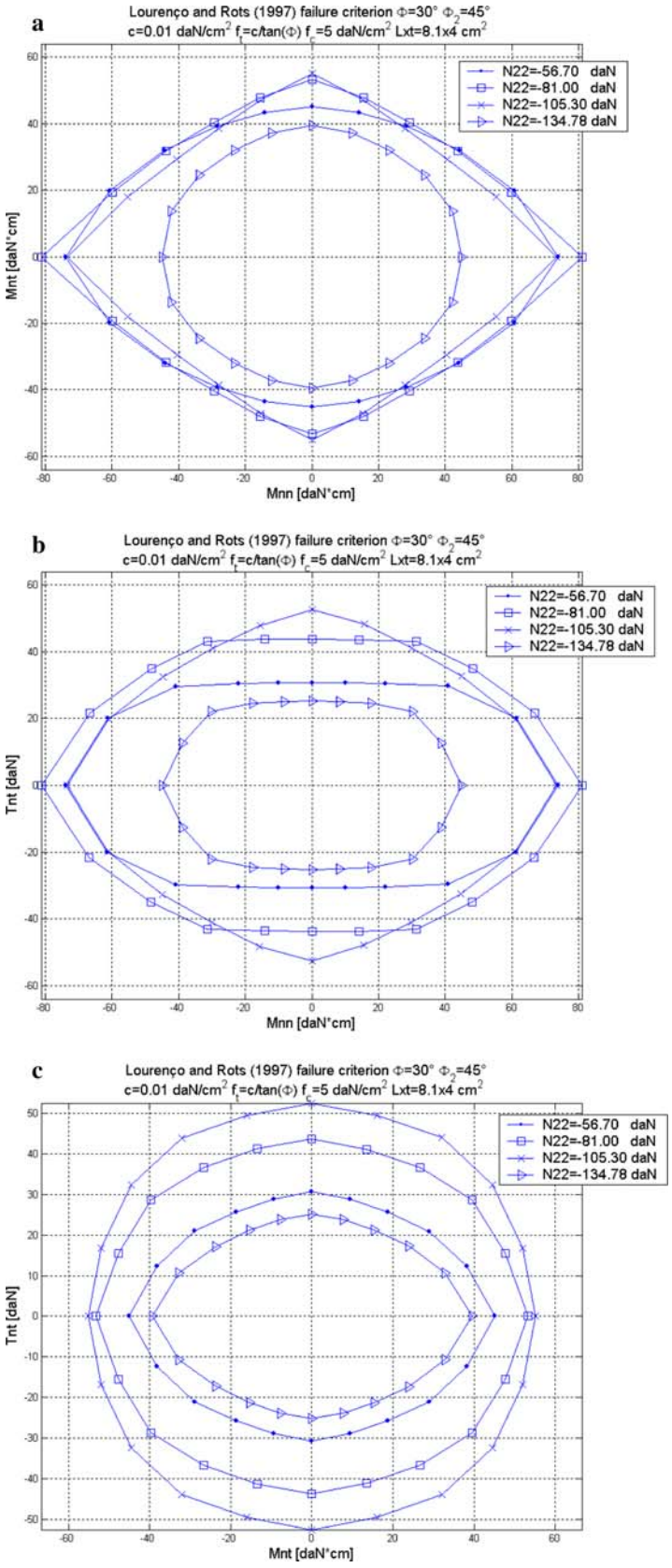

Fig. 8 Interface failure surface sections in presence of different in-plane compressive loads. **a** $M_{nn} - M_{nt}$ sections, **b** $M_{nn} - T_{nt}$ sections **c** $M_{nt} - T_{nt}$ sections. For the interface, a Lourenço and Rots [14] failure criterion ($c = 0.01\,\text{daN/cm}^2, \Phi = 30°, f_c = 5\,\text{daN/cm}^2, \Phi_2 = 45°, f_t = c/\tan(\Phi)$) is adopted

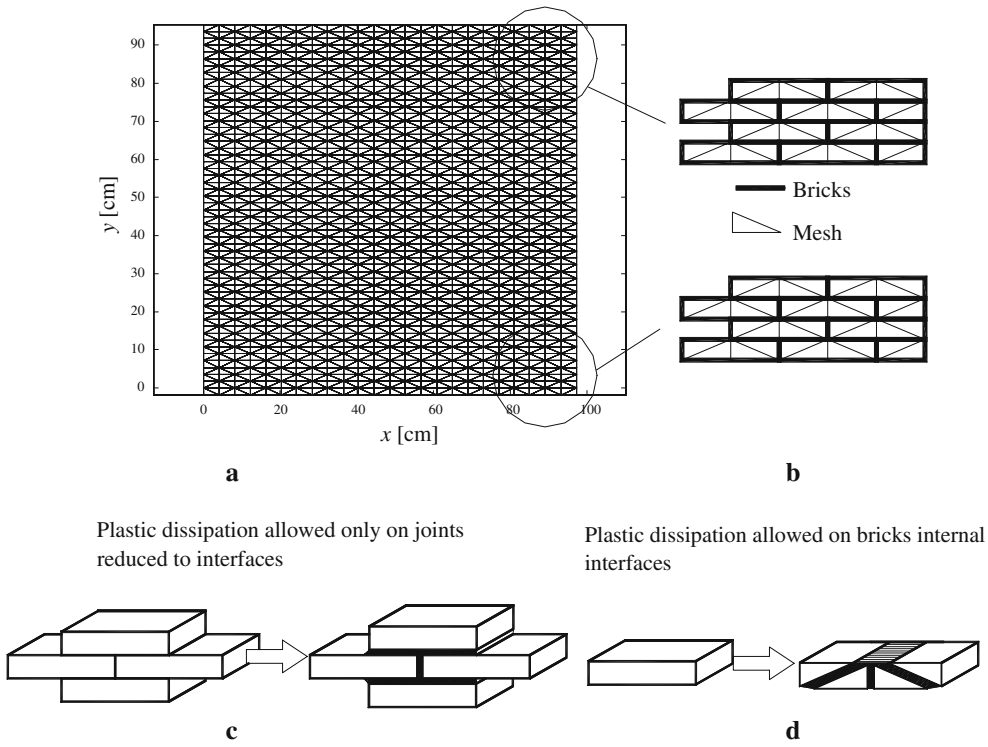

Fig. 9 **a** Mesh used for the heterogeneous analyses reported in the paper (1,375 triangular elements and 2,592 nodes). **b** detail of the mesh, **c** plastic dissipation on joints **d** plastic dissipation on bricks interfaces

in continuum and in the interfaces. $\mathbf{U} = \left[\mathbf{w}\ \tilde{\dot{\boldsymbol{\theta}}}_{nn}\ \tilde{\dot{\boldsymbol{\theta}}}_{nt}\ \tilde{\dot{\boldsymbol{\delta}}}_{zt}\ \dot{\boldsymbol{\lambda}}^{I,\mathrm{ass}}\right]$ is the vector of global unknowns, which collects the vector of assembled nodal velocities ($\mathbf{w}$), the vector of assembled bending interface rotation rates ($\tilde{\dot{\boldsymbol{\theta}}}_{nn}$), the vector of assembled torsion interface rotation rates ($\tilde{\dot{\boldsymbol{\theta}}}_{nt}$), the vector of assembled jumps of velocities on interfaces ($\tilde{\dot{\boldsymbol{\delta}}}_{zt}$) and the vector of assembled interface plastic multiplier rates ($\dot{\boldsymbol{\lambda}}^{I,\mathrm{ass}}$). $\mathbf{A}^{\mathrm{eq}}$ is the overall constraints matrix and collects velocity and rotation boundary conditions, Eq. (1) and constraints for plastic flow in velocity discontinuities.

3 Materials and experimental procedures

In this section, the experimental investigation conducted at the University of Calabria (Italy) on three different series of panel out-of-plane loaded is presented. Each wall, of dimension $100 \times 100\,\mathrm{cm}^2$ (length $\times$ height) was arranged in running bond texture using 1:3 scale bricks and without mortar joints. In-scale models were used in order to reproduce in a simple way a $300 \times 300\,\mathrm{cm}^2$ masonry wall and trying to represent the real behavior of a wall inside a real building. Figure 10 shows the in-scale bricks used, compared to a common Italian brick of

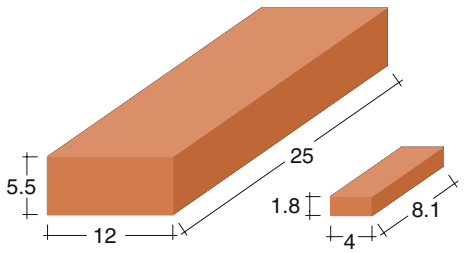

Fig. 10 Prototype and in-scale model comparison

dimensions $25 \times 5.5 \times 12\,\mathrm{cm}^3$. About 54 rows of bricks were utilized, with each row constituted by 12 bricks. The absence of mortar allowed to save time and was economically convenient, since it was possible to use the same bricks for different tests.

Three different series, labeled as Series A, Series B and Series C, were tested, which differ both for the point of application of the out-of-plane load and constraint conditions (Fig. 11). For each series, three different tests were performed, varying the uniformly distributed vertical loads N_{v} applied at the top edge by means of a stiff steel beam. In the first sub-series, labeled as SS 7, N_{v} was kept equal to 7 kN, in the second (SS 10) N_{v} was equal to 10 kN, whereas in the third (SS 13) N_{v} was equal to 13 kN. After the application of the vertical load, a horizontal out-of-plane concentrated force was applied

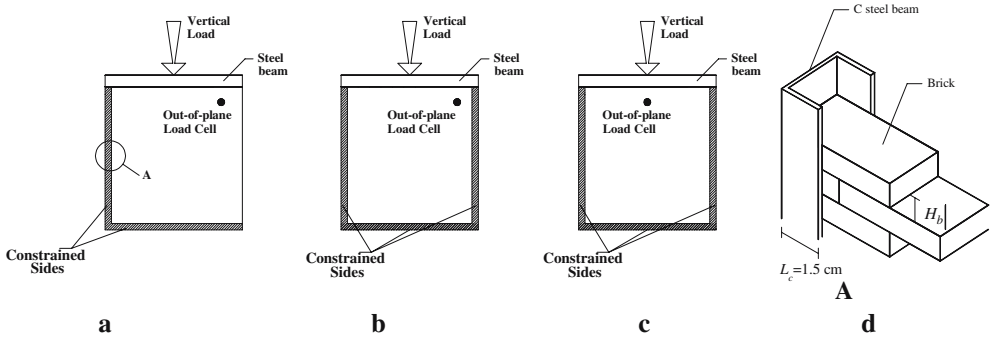

Fig. 11 Loading and constraint conditions. **a** Series A, **b** series B, **c** series C, **d** practical realization of a constrained edge

at a constant rate of 1.3 mm/min perpendicularly to the frontal surface of the panel.

In the first series (Series A), the lower edge and one of the lateral sides of the panels were clamped to a stiff steel frame, whereas the remaining two sides were free both to rotate and move (Fig. 11a). The out-of-plane force was applied in correspondence to the right top edge of the model.

In the second series (Series B), three sides were clamped, whereas the top surface was free to move. Also in this case, the horizontal force was applied eccentrically at the top of the specimens (Fig. 11b).

The third series (Series C) differs from Series B only for the point of application of the out-of-plane load, placed in this case at the top-center of the specimens (Fig. 11c).

Furthermore, it is worth noting that, despite the practical impossibility to realize a perfect clamped edge, a satisfactory technical solution has been adopted using for supports steel profiles with C section of suitable dimensions. As shown in Fig. 11d, the C section of such beams interconnects with bricks, precluding in this way a free rotation, due to the torsional stiffness of the beam. In the numerical model, different boundary conditions were imposed (e.g., clamped and simply supported edges) in order to have an estimation of the influence of the constraints on the collapse load. It was found that limit multiplier does not change considerably. Nevertheless, for vertical edges, a good approximation was found by the authors imposing a limited strength in cylindrical flexion of the edges equal to $M_{nn,e} = (L_c M_{nt,bj} + H_b M_{nn,hj})/H_b$, where $M_{nt,bj}$ is the torsional strength of the bed joint, $M_{nn,hj}$ is the bending strength of the head joint and H_b and L_c are defined in Fig. 11d.

Preliminary mechanical characterization tests were carried out to examine both cohesion and friction angle of dry joints.

Shear tests were carried out on triplet in-scale specimens in order to determine the frictional behavior of dry-joints. Following the European Standard Code (CEN) [6] and using an ad hoc test equipment, specifically designed for this work, cohesion and friction angle of the dry interfaces between two bricks were calculated. Three triplet specimens were subjected to a combined action of pre-compression and shear for three different pre-compression load levels, respectively equal to 0.2, 0.6 and 1.0 N/mm^2. A 100 kN load cell was applied vertically, while a 10 kN load cell allowed the application of the horizontal pressure. The σ-τ diagram obtained is reported in Fig. 12. The straight line has been obtained from a linear regression of the registered τ values for different pre-compression levels.

Experimental tests on the entire panels were conducted in the laboratory by means of a steel frame constituted by four stands made of two U120 steel beams, welded and anchored to ground and connected by means of four U120 beams placed at the top.

The vertical load was applied by means of a hydraulic jack anchored to the frame and equipped with a 20 kN load cell. A stiff steel beam of length 100 cm allowed a uniform distribution of the load above the panel (Fig. 13). The horizontal out-of-plane force was

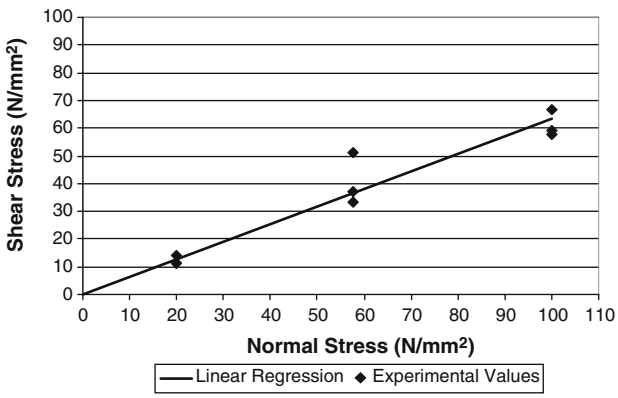

Fig. 12 Experimental friction law for dry-joints

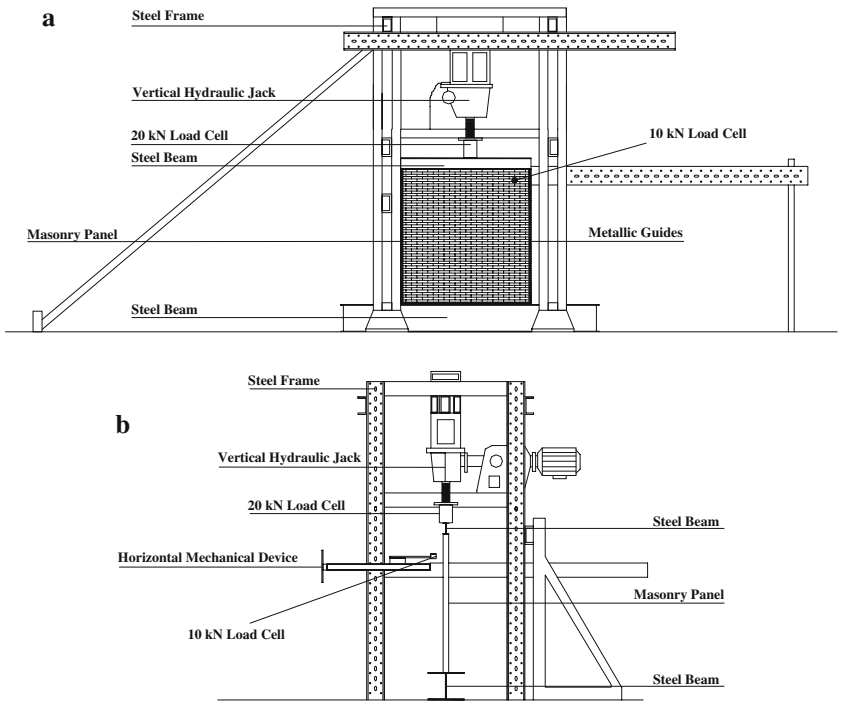

Fig. 13 Steel frame scheme. **a** Front view, **b** lateral view

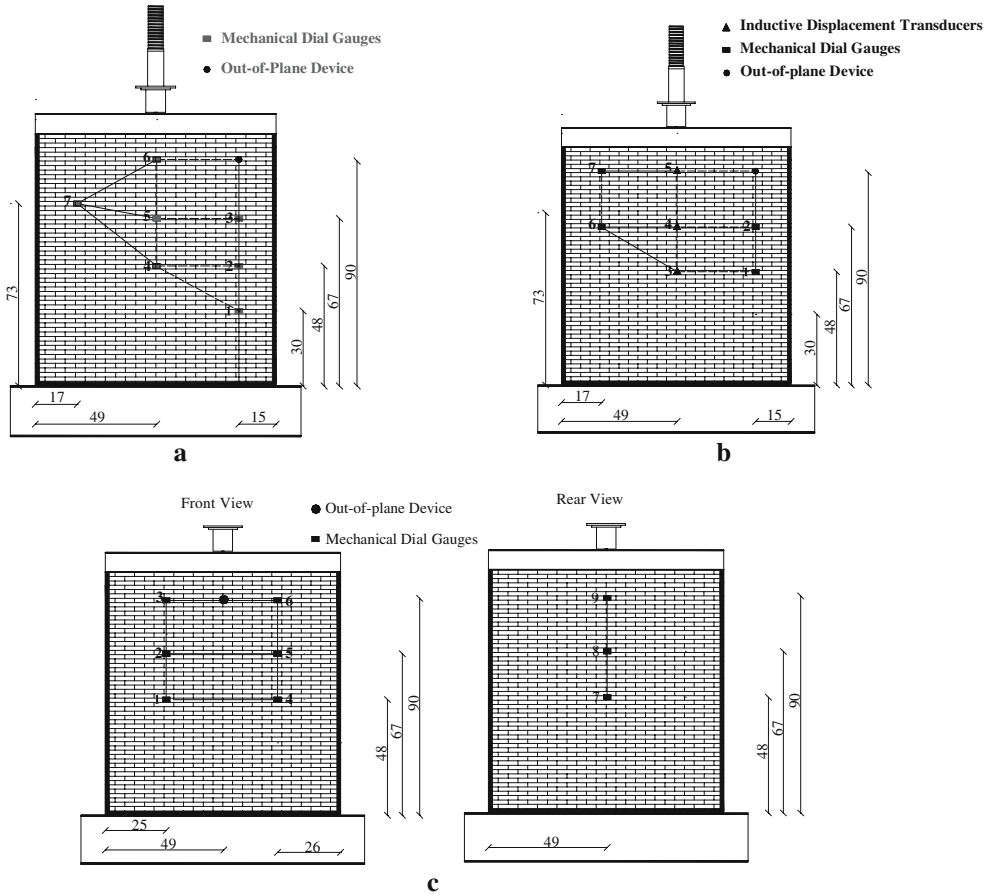

Fig. 14 Instruments position. **a** Series A, **b** series B, **c** series C

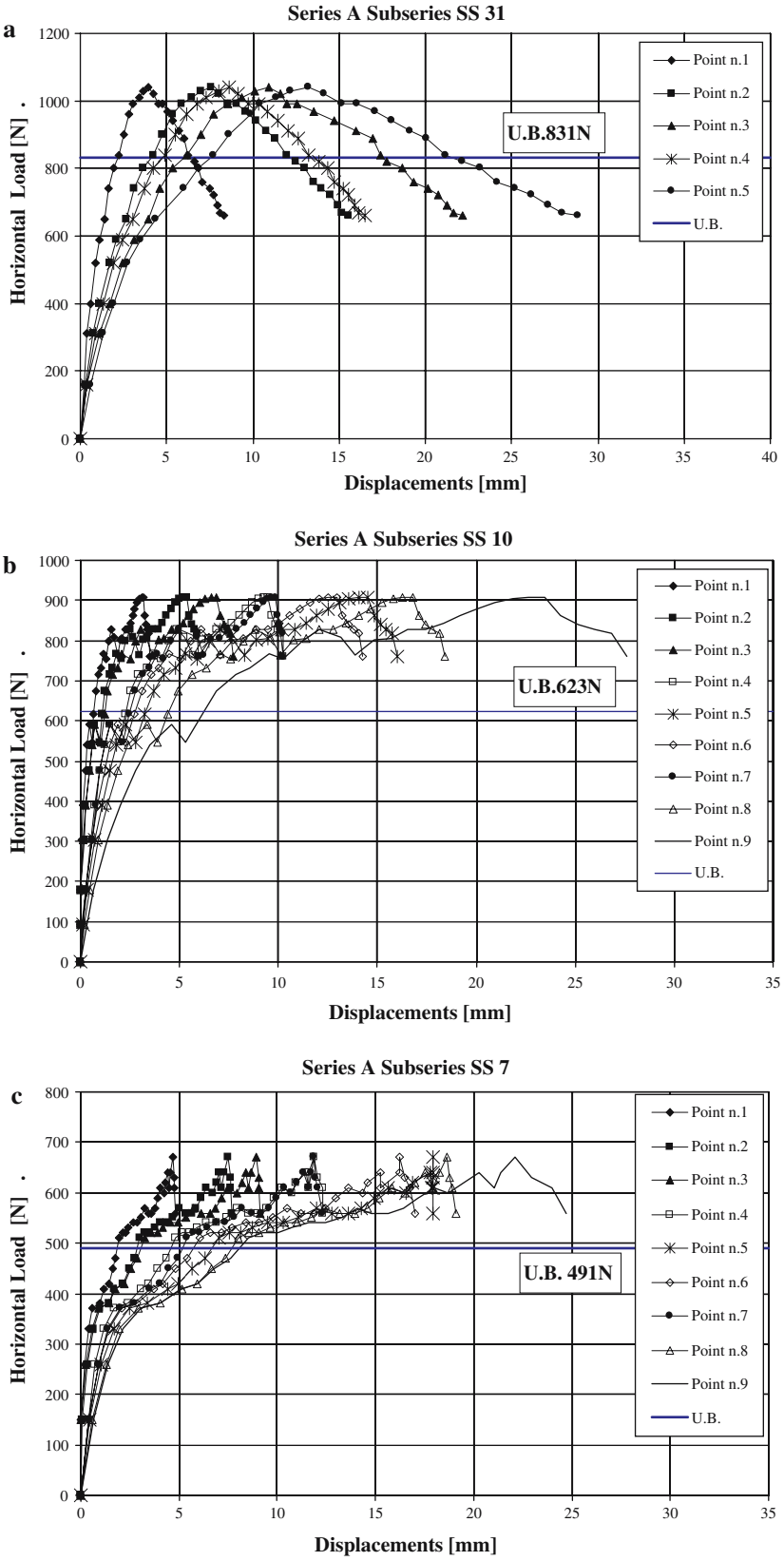

Fig. 15 Load-displacement curves, series A. **a** Series A-SS 13, **b** series A-SS 10, **c** series A-SS 7

applied to the model by means of an ad hoc mechanical device connected to the steel frame, on which a 10 kN load cell was applied. Both load cells were connected to a data-acquiring device in order to register the load values during the test.

The displacement values were registered by means of centesimal mechanically operated dial gauges and linear inductive displacement transducers, placed in different points of the model, see Fig. 14.

4 Comparison between numerical and experimental results

In this section, a comparison between numerical and experimental failure loads is reported for all the series analyzed. Furthermore, a 3D representation of the experimental deformed shape at collapse is shown and a comparison between numerical and experimental failure mechanisms is given. It is worth noting that, for each sub-series, at least three panels have been tested. Nevertheless, for the sake of conciseness, load-displacement curves relative to the investigated points are reported only for one panel of each sub–series.

As concerning the numerical analysis, a linearization with 44 planes for each interface between adjacent triangles is implemented in the FE upper bound limit analysis code, using a Mohr–Coulomb failure criterion with friction angle equal to 30 ° and cohesion equal to 0.01 N/mm^2 for mortar joints interfaces. Such data are derived from experimental data collected on dry-joints (see Fig. 12), nevertheless a non-null value for cohesion is chosen with the aim of avoiding possible numerical instabilities for head joints in solving the optimization problem (11).

It is worth noting that a full parametric study in terms of mortar friction angle, cohesion, compressive strength and tensile strength of dry-joints could be useful for a full characterization of experimental evidences. This analysis is a work in progress by the authors and is not reported here for all the Series analyzed for the sake of conciseness.

Finally, it is stressed that both deformed shapes at collapse and failure loads obtained with the present model are in excellent agreement with experimental data. Furthermore, the model proposed has the following advantages if compared with other models presented in the technical literature (as for instance those based on homogenization, see Milani et al. [17]): (a) is able to give a point by point description of the failure mechanism, which usually zigzags between adjacent bricks, (b) is able to reproduce the important role at failure of sliding and (c) can be used for both thick and thick plates even when the size of the bricks is not small if compared with the size of the panel. In particular, it is worth underlining that the reproduction of failure modes involving bricks sliding is not possible when classic plate approaches based on Munro and Da Fonseca [18] model are used (see for instance Casolo [3]).

4.1 Series A

For Series A SS 13 the experimental collapse load reached was approximately equal to 1,000 N, for Series A SS 10 approximately 800 N, for Series A SS 7 approximately 550 N. A comparison between numerical upper bound failure loads and experimental load-displacements curves is reported for all the sub-series in Fig. 15. In all the cases analyzed, the difference between the experimental and numerical ultimate loads is less than

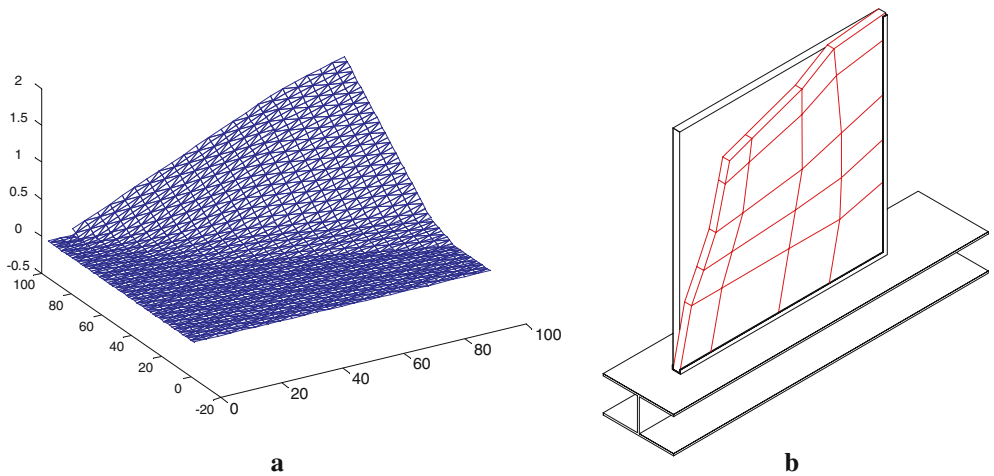

Fig. 16 Comparison between numerical (**a**) and experimental (**b**) collapse mechanisms, series A

20%, demonstrating that technically meaningful results can be obtained with the model proposed.

Experimental evidence shows that the collapse mechanism of this series involves the diagonal upper part of the specimens. In particular, during tests, a triangular upper portion of the wall (the free sides) moved, rotating around an inclined cylindrical hinge, whereas the lower part of the panel was not involved in the failure mechanism, due to the constraint condition (Fig. 16). This is reproduced by the numerical model, as shown in Fig. 16a and b, where a comparison between numerical and experimental deformed shapes at collapse is reported. As one can note, both collapse loads and failure mechanisms demonstrate the reliability of the numerical model proposed.

A parametric study for one of the panels constrained on two sides (Series A Subseries SS 13) is finally reported in Fig. 17 varying friction angle of dry-joints and maintaining cohesion equal to 0.01 N/mm^2. In Fig. 17 from a to d deformed shapes at collapse of Series A SS 13 for friction angles Φ, respectively, equal to $10°, 20°, 30°$ and $40°$ are reported. Black lines underlining the failure

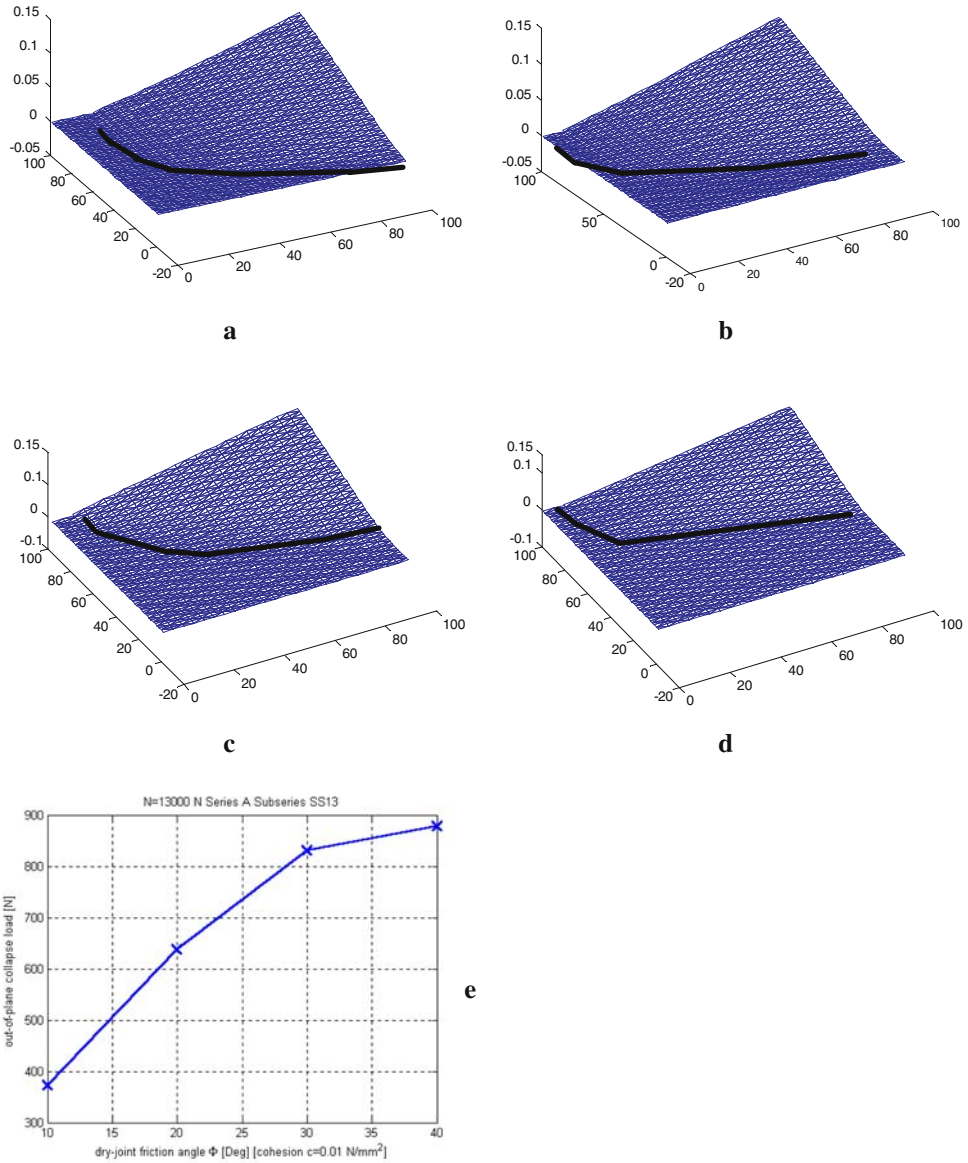

Fig. 17 Deformed shapes at collapse (from **a** to **d**) and collapse loads (**e**) of Series A Subseries SS 13 at different values of dry-joints friction angle. The parametric study is conducted varying mortar friction angle (**a** $\Phi = 10°$, **b** $\Phi = 20°$, **c** $\Phi = 30°$, **d** $\Phi = 40°$) and maintaining cohesion equal to 0.01N/mm^2. *Black lines* approximately delimitate failure mechanism

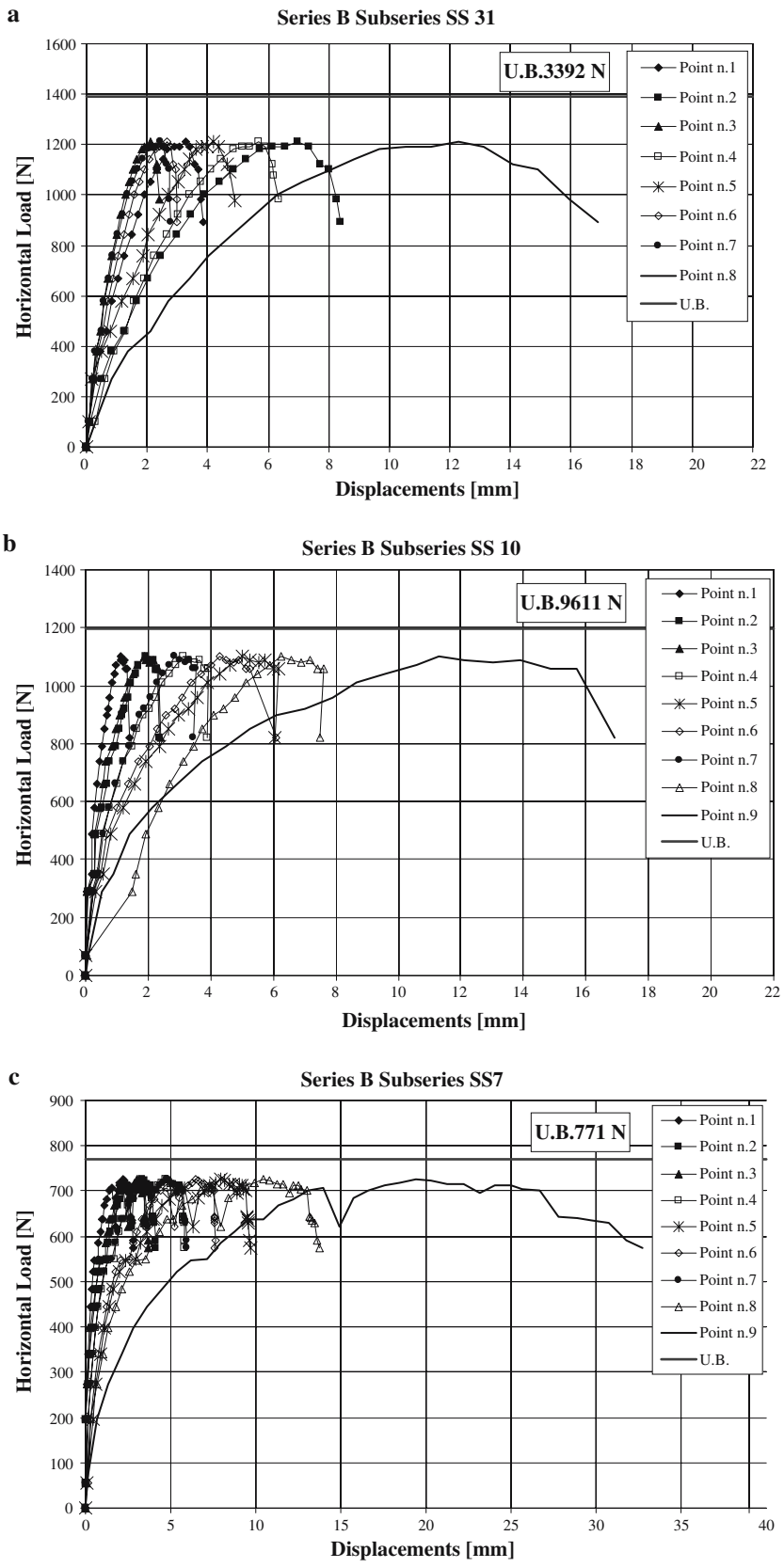

Fig. 18 Load-displacement curves, series B. **a** Series B-SS 13, **b** series B-SS 10, **c** series B-SS 7

mechanism are also represented. It is worth noting that the portion of the wall involved in the failure mechanisms reduces and changes considerably its shape when Φ is increased from 10° to 40°. Finally, in Fig. 17e the failure load of the structure obtained numerically is reported for each friction angle analyzed. As one can note, the failure load remains in practice constant for sufficiently high values of Φ.

4.2 Series B

In the second series, three sides of the panels were fixed to the frame, so that only their upper edge was free to rotate and move. Also in this case, the horizontal load was applied eccentrically, in correspondence to a corner of the specimens (Fig. 11b).

For Series B SS 13 the horizontal collapse load reached was approximately equal to 1,200 N, for Series B SS 10 approximately 1,100 N, for Series B SS 7 approximately 700 N.

A comparison between collapse loads experimentally and numerically evaluated is reported in Fig. 18. In all the cases analyzed, excellent agreement is found. Finally, a comparison between experimental and numerical failure mechanisms is reported in Fig. 19. In this case, the area involved by the cracks is restricted to the zone near the point of application of the horizontal device, because of the different constraint conditions with respect to the previous case. The reliability of the numerical results should be noted. In particular, the numerical deformed shape at collapse reproduces very well the out-of-plane sliding of the bricks in correspondence to the point of application of the load, see Fig. 20.

4.3 Series C

Panels belonging to series C were arranged with the same boundary conditions described for the previous series. Differently from the previous case, the point of application of the horizontal force was placed at the top center of the panels (Fig. 11c).

In this case, four different specimens were tested. For Series C SS 13 the horizontal collapse load reached was approximately equal to 1,300 N, for Series C SS 13 approximately 850 N, for Series C SS 7 approximately 800 N.

A comparison between experimental and numerical collapse loads is reported in Fig. 21. In all the cases analyzed, excellent agreement is found. Finally the deformed shape at collapse of the panels is shown in Fig. 22. The failure mechanism is similar to that obtained

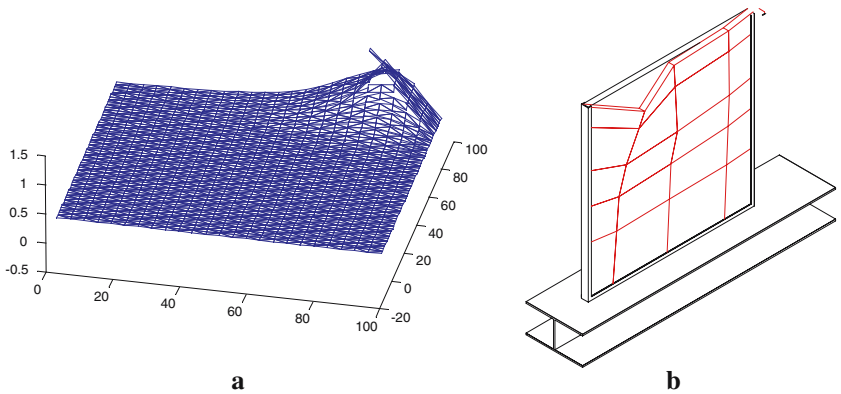

Fig. 19 Comparison between numerical (**a**) and experimental (**b**) collapse mechanisms, series B

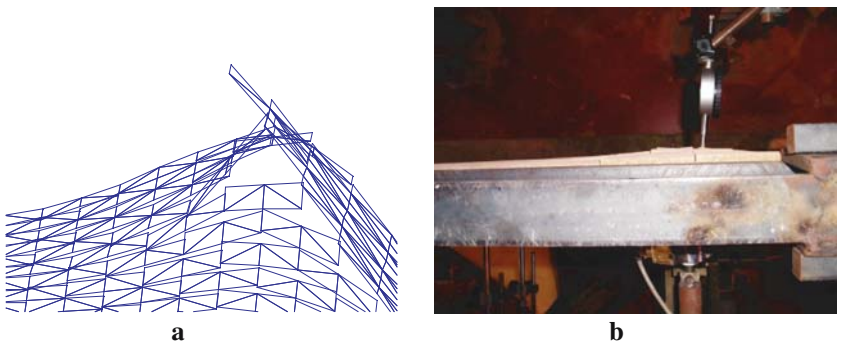

Fig. 20 Series B, detail of failure mechanism in correspondence to the point of application of the load. **a** Numerical, **b** experimental

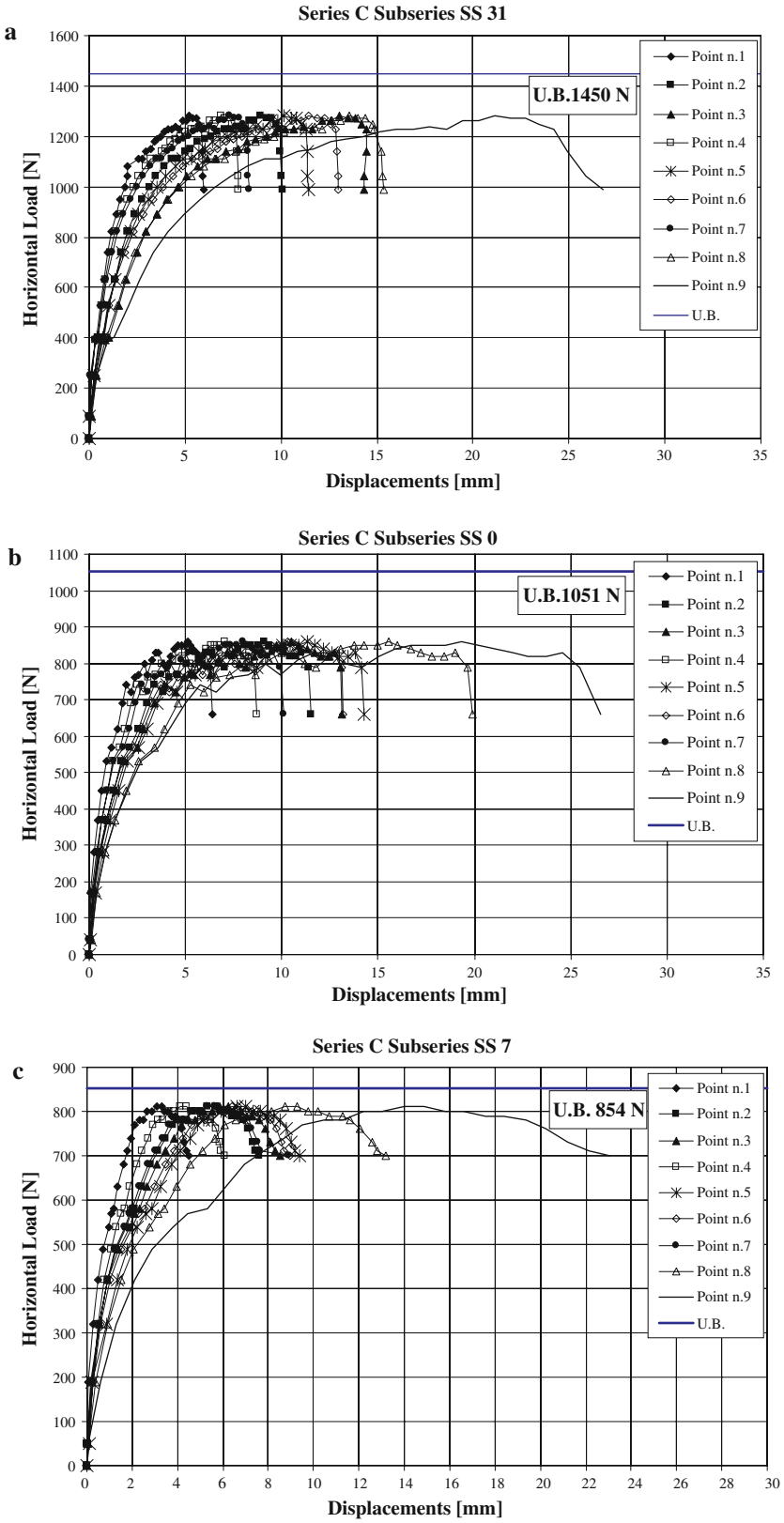

Fig. 21 Load-displacement curves, series C. **a** Series C-SS 13, **b** series C-SS 10, **c** series C-SS 7

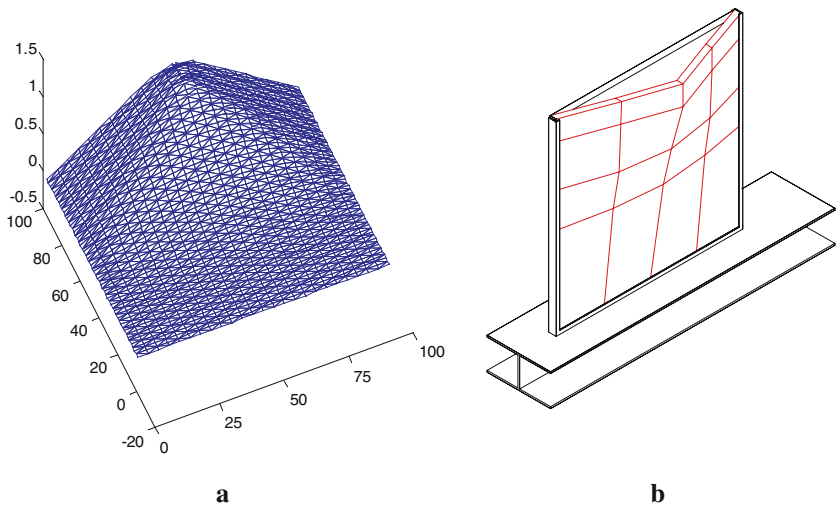

Fig. 22 Comparison between numerical (**a**) and experimental (**b**) collapse mechanisms, series C

for series B, except for the different position of the plastic hinges.

5 Conclusions

A heterogeneous upper bound FE model for the limit analysis of out-of-plane loaded masonry walls has been presented. Numerical results for three different series of masonry panels out-of-plane loaded have been compared with experimental data collected at the University of Calabria. Experimentation has been carried out with the aim of studying the collapse mechanisms of dry-joint masonry subjected to out-of-plane actions (e.g., wind, earthquake, explosions).

For all the series analyzed, FE limit analysis results fit the experimental data well, both for that which concerns failure mechanisms and for that which concerns ultimate loads.

Acknowledgments A.Tralli and G.Milani gratefully acknowledge the support of the research project MIUR COFIN 2005—Resistenza e degrado di interfacce in materiali e sistemi strutturali. Coordinator: Prof. A. Corigliano. R.S. Olivito and F.A. Zuccarello gratefully acknowledge the support of the research project ex MURST 60% 2006—Analisi sperimentale di pareti murarie soggette a carichi fuori dal piano. Coordinator: Prof. R.S. Olivito.

References

1. Borri A, Avorio A, Cangi G (2001) Guildelines for seismic retroffiting of ancient masonry buildings. Rivista italiana di geotecnica 4:112–121
2. British Standard Institution (2002) Code of practice for use of masonry. Structural use of unreinforced masonry. BS 5628–1:1992, London
3. Casolo S (1999) Rigid element model for non-linear analysis of masonry facades subjected to out-of-plane loading. Commun Numer Methods Eng 15(7):457–468
4. Cecchi A, Milani G, Tralli A (2006) A Reissner-Mindlin limit analysis model for out-of-plane loaded running bond masonry walls. Int J Solids Struct (in Press)
5. CEN-European Commiteee for Normalization (2004) Design of masonry structures. Common rules for reinforced and unreinforced masonry structures. EN 1996-1-1:2002, Eurocode 6, Brussels, Belgium
6. CEN-European Commiteee for Normalization (2003) Methods of tests for masonry—determination of initial shear strength. prEN 1052–3
7. Chee Liang NG (1996) Experimental and theoretical investigation of the behavior of brickwork cladding panel subjected to lateral loading. PhD Thesis, University of Edinburgh, Scotland
8. Gazzola EA, Drysdale RG (1986) A component failure criterion for blockwork in flexure. In: Anand SC (ed) Proceedings of structures '86 ASCE, New Orleans, pp 134–153
9. Gazzola EA, Drysdale RG, Essawy AS (1985) Bending of concrete masonry walls at different angles to the bed joints. In: Proceedings of 3th North American Masonry conference Arlington, Paper 27
10. Guggisberg R, Thurlimann B (1988) Failure criterion for laterally loaded masonry walls: experimental investigations. In: Proceedings of 8th International brick/block Masonry conference, Ireland
11. Guggisberg R, Thurlimann B (1990) Failure criterion for laterally loaded masonry walls. In: Proceedings of 5th North American Masonry conference, pp 949–958
12. Krabbenhoft K, Lyamin AV, Hjiaj M, Sloan SW (2005) A new discontinuous upper bound limit analysis formulation. Int J Numer Methods Eng 63:1069–1088
13. Lourenço PB (2000) Anisotropic softening model for masonry plates and shells. ASCE J Struct Eng 126(9):1008–1016
14. Lourenço PB, Rots J (1997) A multi-surface interface model for the analysis of masonry structures. ASCE J Eng Mech 123 (7):660–668
15. Milani G, Lourenço PB, Tralli A (2006) Homogenised limit analysis of masonry walls. Part I: failure surfaces. Comput Struct 84:166–180

16. Milani G, Lourenço PB, Tralli A (2006) Homogenised limit analysis of masonry walls. Part II: structural examples. Comput Struct 84:181–195
17. Milani G, Lourenço PB, Tralli A (2006) Homogenization approach for the limit analysis of out-of-plane loaded masonry walls. ASCE J Struct Eng 132(10):1650–1663
18. Munro J, Da Fonseca AMA (1978) Yield-line method by finite elements and linear programming. ASCE J Struct Eng 56B:37–44
19. Nadai A (1950) Theory of flow and fracture of solids. The problem of plastic torsion. In: Experimental representation of stress distribution, Chap. 35. McGraw-Hill, New York
20. Olivito RS, Zuccarello FA (2006). Indagine sperimentale sul comportamento meccanico di pareti murarie caricate fuori dal piano (Experimental analysis on the mechanical behavior of masonry walls out-of-plane loaded). In: Proceedings of XXXV national conference AIAS, Ancona
21. O.P.C.M. 3431/05 09/05/2005 (2005) Ulteriori modifiche ed integrazioni all'OPCM 3274/03 and O.P.C.M. 3274, 20/03/2003, Primi elementi in materia di criteri generali per la classificazione sismica del territorio nazionale e di normative tecniche per le costruzioni in zona sismica (in Italian).
22. Orduna A, Lourenço PB (2005) Three-dimensional limit analysis of rigid blocks assemblages. Part I: torsion failure on frictional interfaces and limit analysis formulation. Int J Solids Struct 42(18–19):5140–5160
23. Rondelet JB (1802) Traité théorique et pratique de l'art du batir. Paris
24. Sinha BP (1978) A simplified ultimate load analysis of laterally loaded model orthotropic brickwork panels of low tensile strength. Struct Eng 56B(4):81–84
25. Sloan SW (1988) Lower bound limit analysis using finite elements and linear programming. Int J Numer Anal Method Geomech 12:61–77
26. Spence R, Coburn A (1992) Strengthening building of stone masonry to resist earthquakes. Meccanica 27:213–221
27. Sutcliffe DJ, Yu HS, Page AW (2001) Lower bound limit analysis of unreinforced masonry shear walls. Comput Struct 79:1295–1312
28. Van Der Pluijm R (1999) Out-of-plane bending of masonry. Behaviour and strength. PhD Thesis, Eindhoven University of Technology, The Nederlands
29. West HWH, Hodgkinson HR, Haseltine BA (1977) The resistance of brickwork to lateral loading. Struct Eng 55(10): 442–430